pp 1291–1314. © Royal Aeronautical Society 2016
doi: 10.1017/aer.2016.54

Morphing structure for a rudder

M. A. Castillo-Acero
miguelangel.castillo@aernnova.com
Aernnova, C. Princesa de Éboli
Madrid
Spain

C. Cuerno-Rejado
Escuela Técnica Superior Ingenieros Aeronáuticos
UPM
Madrid 28040
Spain

M. A. Gómez-Tierno
Escuela Técnica Superior Ingenieros Aeronáuticos
UPM
Madrid
Spain

ABSTRACT

The modification of aerofoils with structural morphing in order to enhance aerodynamic efficiency is an active field of research. The required forced and induced displacements are, usually, out the current developments on shape memory alloys, piezoelectric actuators or multi-stable structures for commercial transport aircraft applications. This work aims to present studies for obtaining an optimum rudder structure which morphs to a pre-defined curvature that can sustain aerodynamic and internal loads in a critical certification load case for a commercial transport aircraft. It also includes the feasibility of a morphing rudder based on a zero Poisson skeleton, or close to a zero Poisson ratio panel geometrical configuration that has no transverse deformation when perpendicularly loaded and which is produced with an additive layer manufacturing process.

Keywords: morphing; structures; vertical stabilizer; rudder; zero Poisson skeletons, additive layer manufacturing

Received 3 March 2015; revised 4 August 2015; accepted 23 February 2016; first published online 20 June 2016.

https://doi.org/10.1017/aer.2016.54 Published online by Cambridge University Press

NOMENCLATURE

b	distance between stringers
c	chord, length
c_L	aerodynamic lift coefficient
d, h	distances
E	Young modulus
F	Farrar factor
G	shear modulus
k	proportionality constant
k_s	ratio, stringers thickness vs. springs
$l(y)$	lifting forces per unit, span
$m(z)$	bending moments per unit, span
p	pressure
t	skin thickness
t_s	stringers thickness
v	velocity
x	distance
α, θ	angles
ρ	fluid, air, density
σ	stress
υ	Poisson ratio

1.0 INTRODUCTION

This paper demonstrates the feasibility of an innovative morphing rudder that presents enhanced aerodynamic efficiency. This work includes the structural definition of the non-conventional rudder whose enhanced aerodynamic characteristics were previously analysed[1]. The aerodynamic improvements that can be achieved with an unconventional morphing rudder have already been quantified. The geometry of such a rudder provides a continuous curvature function between the trailing edge, both sides of the vertical stabilizer fixed part and the rudder, and the function follows curving the rudder body itself. The curves on previous study were obtained by means of graphical approaches to achieve a theoretical shape. In this study, we develop a morphing feasible structure to obtain a close solution to the theoretical aerodynamic optimum shape.

Achieving the curved shapes needed to obtain the aerodynamic enhancements requires sufficient capacity on the actuation system. This capacity essentially translates into two parameters: the displacements required at different points, and actuator forces to maintain the shape under loading. While in recent years there have been numerous developments in the fields of actuators, e.g. shape memory, or multi-stable piezoelectric materials[2-4], in this work we prefer to develop a system based on commercially available actuators. The focus of this study is on developing the structure based on articulated ribs with highly deformable panels, chord-wise direction, and enough stiffness and strength span-wise to able to sustain the internal loads per certification requirements. To complete the new rudder architecture, a highly deformable elastomeric rubber coating is required to provide non- permeability to air. The literature contains good examples of this type of structure[5], although its application is focused on developing a solution for wing spoilers where deflections are fairly lower ($\pm 15°$)

https://doi.org/10.1017/aer.2016.54 Published online by Cambridge University Press

Table 1
Visijet M3 X 3D printable material properties[14]

Properties	Condition	VisiJet M3X
Density at 80°C (liquid)	ASTM D4164	1.04 g/cm^3
Tensile strength	ASTM D638	49 MPa
Tensile modulus	ASTM D638	2,168 MPa
Elongation at break	ASTM D638	8.3%
Flexural strength	ASTM D638	65 MPa
Heat distortion at 0.45 Mpa	ASTM D648	88°C

than in the rudder (±30°, the typical values for this study). This concept has been also refined for wing lift devices (flaps)[6].

The present study includes two main objectives: the optimum articulated rib configuration geometry and the definition of the highly deformable skin panels. These panels are cell-skeleton-based and highly orthotropic. They are often called Poisson zero skeletons in the literature, defined as close-to-zero Poisson ratio panels based on stiffeners in one direction, and in the perpendicular direction, geometrical cells that behave as springs. Studies on these panels have been found for wind turbine blade applications[7-9]. There are also studies of their introduction on aircraft, such as for active aero-elastics,[10-12] or a more general overview[13].

The approach for obtaining the equations to derive the optimum configuration has been the structural pre-sizing. The load case selected is the one-engine-out that usually is critical for the sizing of the rudder for commercial transport aircraft with pod-mounted engines under the wing. The articulated-ribs concept is based on aluminium 7X series riblets that rotate to provide the required shape. The turning law at each articulation and the riblets-length geometry is selectable. Different configurations for the zero Poisson highly deformable skeleton have also been considered. Then it is necessary to obtain stiffness/strength properties, both in-plane orthotropic $E_1, E_2, G_{12}, \upsilon_{12}, \upsilon_{21}$ and out-plane $E_3, G_{13}, G_{23,}\upsilon_{13}, \upsilon_{31}\upsilon_{23}, \upsilon_{32}$. The raw material considered is Visijet M3 X properties in Table 1. This material can be easily processed in a commercially available 3D printing device and therefore can be defined as a printable material. A material is 3D-printable if can be the raw material for an additive layer manufacturing process.

The application of this type of morphing rudder means potential weight savings in commercial transport aircraft empennages, thus representing an important opportunity for aircraft OEMs and Tier 1 suppliers that design and build these types of structures. The more efficient the rudder, the smaller it can be and the less it will weigh. This is an important finding due to the trend in aeronautical research for more efficient aircraft with lower fuel consumption, as well as requirements for reduction of CO_2 emissions.

2.0 METHODOLOGY

The methodology is based on the preliminary sizing of the new non-conventional rudder. The applied external loads considered come from previous studies[1] for the load case of engine failure during takeoff that requires maximum rudder deflection of 30°. In commercial transport aircraft under the wing engines pod configuration, this load case usually sizes

https://doi.org/10.1017/aer.2016.54 Published online by Cambridge University Press

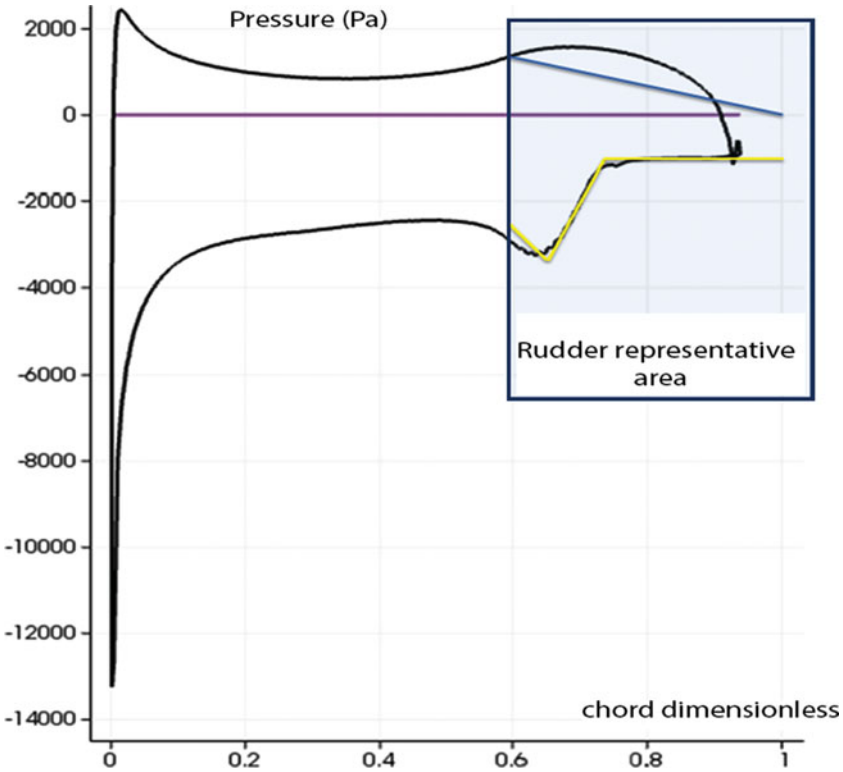


Figure 1. (Colour online) Aerodynamic loads on the morphing rudder and rest of the vertical tail plane[1] section one-third height.

the rudder. The load case of crosswind landing yields similar loading and practically the same order of criticality. From the previous study, the differential pressure distribution in the vertical tail plane section at one-third height Vertical Tail Plane (VTP) span has been obtained (Fig. 1). Then the loading at the morphed rudder with a linear approach is considered (Fig. 2).

These aerodynamic loads are translated into:

- *l(y)*: lifting forces per unit span length, in this case lateral 'y' forces
- *m(z)*: 'z' bending moments per unit span length

$$l(y) = \frac{1}{2}\rho v^2 c \sum^{c_l} \left(x_{il_c}\right) \Delta \left(x_{il_c}\right), \quad \ldots (1)$$

$$m(z) = \frac{1}{2}\rho v^2 c^2 \sum^{c_l} \left(x_{il_c}\right) \left(x_{il_c} - x_{l/c}\right) \Delta \left(x_{il_c}\right) \quad \ldots (2)$$

These loads are discretised along the rudder span in eight zones. Then, following a classical bending/torsion box strength analysis approach, the critical internal loads in the morphed rudder structure and the maximum reactions at the fittings with the fixed vertical stabilizer part are derived.

https://doi.org/10.1017/aer.2016.54 Published online by Cambridge University Press

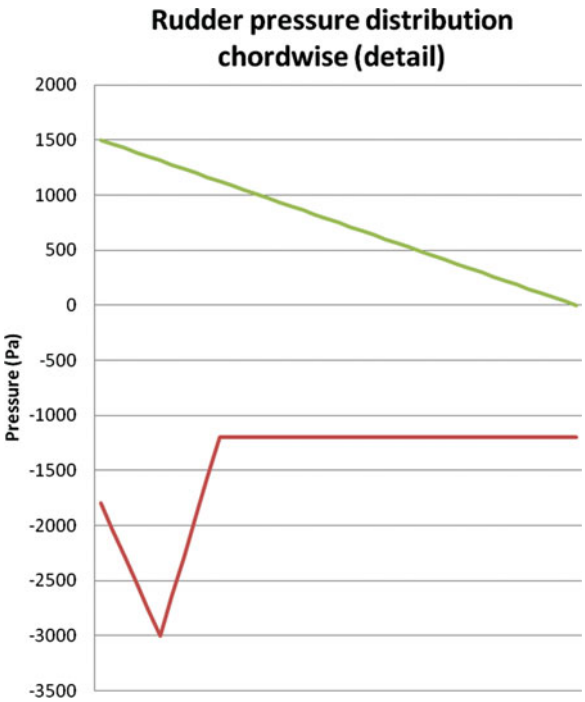


Figure 2. (Colour online) Aerodynamic loads model on the morphing rudder.

2.1 Articulated ribs geometry

The kinematic of the morphing rudder is based on articulated ribs composed of riblets that rotate when actuated (Fig. 3). An optimisation study of the number and configuration of these riblets is performed. The configuration with more riblets results in better adaptation to the target curve shape and therefore better aerodynamic efficiency. However, this approach increases the weight. The optimum is achieved balancing these two trends. Also in this case under study due to high rudder deflections to be considered ($\pm 30°$) there is non-linearity that needs to be analysed with in adequate approach and detail.

The rotation law relationship between the angle turned by one riblet and the next with respect to its initial position is defined. The law of rotation at each joint can be imposed by the limitations of the mechanism of action, but as the mechanism itself is not the focus of this study, a mathematical equation for rotation type that can then be physically feasible and functionally tested is proposed. One simple rotation equation is a geometrical one, where the angle rotated by a rib is proportional to the angle of the previous rib. The proportionality constant is k_1, and θ is the angle rotated by the riblets, with subscript i the identifier of each riblet. Figure 3 depicts the parameters involved.

$$\theta_{i+1} = k_1 \theta_i \qquad \ldots (3)$$

This equation can also express the angle rotated by the riblet i depending on the angle rotated by the first rib:

$$\theta_i = (k_1)^i \theta_0 \qquad \ldots (4)$$

https://doi.org/10.1017/aer.2016.54 Published online by Cambridge University Press

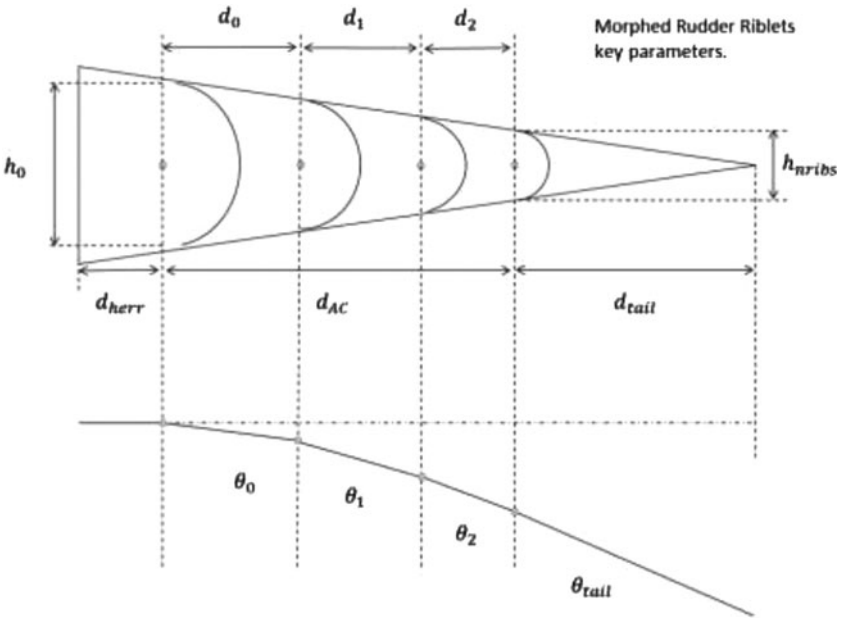


Figure 3. Geometry parameters for articulated ribs.

It also establishes the proportionality relationship between the length of a rib and the previous one by a geometric progression constant k_2 with d_i the length from the centre of the rib joint i to the centre of the rib joint i + 1.

$$d_{i+1} = k_2\, d_i \qquad \ldots (5)$$

$$d_i = (k_2)^i d_0 \qquad \ldots (6)$$

So far, four parameters that define this study target have been identified: d_0, θ_0, k_1 and k_2. The number of ribs, n_{ribs}, is also added, as are the length between the rear spar and the first joint d_{herr}, and the tail length d_{tail}.

There are certain constraints that reduce the number of parameters. The sum of the lengths of all the riblets, the tail and the first riblet or fitting must be equal to the length of the rudder:

$$d_{AC} = d_{herr} + d_{tail} + \sum_0^{n_{ribs}} d_i \qquad \ldots (7)$$

There is also a relationship between the accumulated length of the riblets and the proportionality constant using the summation of a geometric progression of the ratio k_2 and first element d_0:

$$\sum_0^{n_{ribs}} d_i = d_0 \sum_0^{n_{ribs}} (k_2)^i = d_0 \frac{(k_2)^{n_{ribs}} - 1}{k_2 - 1}, \qquad \ldots (8)$$

$$d_{AC} = d_{herr} + d_{tail} + d_0 \frac{{k_2}^{n_{ribs}} - 1}{k_2 - 1} \qquad \ldots (9)$$

https://doi.org/10.1017/aer.2016.54 Published online by Cambridge University Press

This means that the parameters are coupled and therefore a degree of freedom is lost.

We impose the condition that the deflecting rotation must be equivalent to 30° to obtain an additional coupling as follows:

$$d_{AC}\sin 30 = d_{herr}\sin 0 + d_{tail}\sin\theta_{tail} + \sum_{0}^{n_{ribs}} d_i \sin\theta_i \qquad \ldots(10)$$

Therefore,

$$\frac{d_{AC}}{2} = d_{tail}\sin\theta_{n_{ribs}+1} + \sum_{0}^{n_{ribs}} (k_2)^i d_0 \sin\left((k_1)^i\theta_0\right) \qquad \ldots(11)$$

There is another consideration that further reduces the number of variables. The geometry of the control surface presents diminishing heights along the chord. This leads us to define a binding relation between the height and the length of each rib that can be expressed as:

$$\frac{d_0}{h_0} = \frac{d_0 k_2}{h_1} = \frac{d_0 (k_2)^2}{h_2} \cdots = \frac{d_0 (k_2)^{n_{ribs}}}{h_{n_{ribs}}} \qquad \ldots(12)$$

Calling the tail half-angle α:

$$h_0 = h - d_{herr}\sin\alpha, \qquad \ldots(13)$$

$$h_{n_{ribs}} = d_{tail}\sin\alpha, \qquad \ldots(14)$$

$$\alpha = \tan^{-1}\frac{h}{d_{AC}} = \sin^{-1}\frac{h}{l} \qquad \ldots(15)$$

Therefore,

$$\frac{h_{n_{ribs}}}{h_0} = \frac{d_{tail}\sin\alpha}{h - d_{herr}\sin\alpha} = (k_2)^{n_{ribs}} \qquad \ldots(16)$$

This gives us the law of proportionality for the homothetic riblets once the number of ribs is selected. Introducing this into the above equation results in d_0. To avoid complexities in the mechanism and avoid penalising the weight, the process is started with three ribs which are added to the tail, so the fitting involves four joints. The values of the parameters obtained to define the geometry of the first articulated rib are shown below, with the angle values in radians and the distances in meters. The results are included in Table 2.

2.2 Skins span-wise

Skins are cell-based skeletons that span-wise present higher stiffness than chord-wise.

https://doi.org/10.1017/aer.2016.54 Published online by Cambridge University Press

Table 2
Articulated ribs results

n_{ribs}	k_2	θ_{tail}	$\Delta\theta$	θ_0	$h_{n_{ribs}}(m)$
3	0, 61	0, 35	0, 15	0, 3	0, 1
h_0 (m)	d_{AC} (m)	$d_0(m)$	$d_{herr}(m)$		$d_{tail}(m)$
0, 27	0, 8	0, 3	0, 13		0, 2

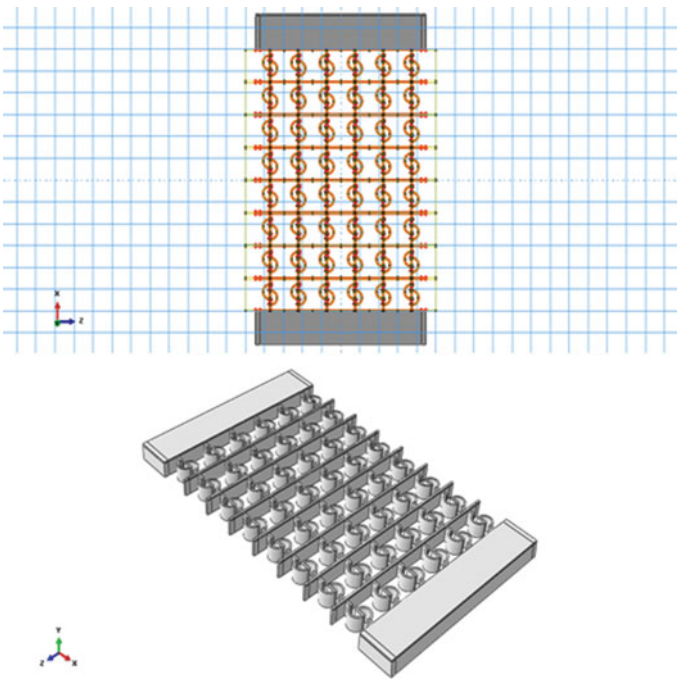


Figure 4. (Colour online) double-C skeleton- skin panels.

Two different geometric configurations seeking to maximise the elastic module E_1, E_2, E_3 with minimum weight are considered. The chord-wise direction corresponds to the X axis or Direction 1 in these studies; the Y axis corresponds to the thickness (Direction 2) and the Z axis to span-wise direction (Direction 3). The two configurations are a novel 'double C' Fig. 4 and 'V straight' (Fig. 5). The latter can be found in the literature[15] and it is composed of two straight segments that form a given angle within the parameter for orthotropic characterisation with the stiffeners. The new double C is composed of two connected curved segments. The radius of these curved members is the parameter for defining the orthotropic behaviour of the panel, as is the presence of a connecting straight segment between the curved members and the length. We analyse whether this novel double-C configuration, keeping the basic common geometric features, shows improvements in terms of specific elastic modulus in relation to the V-straight configuration.

The skins sizing critical span-wise condition is compression load. For the compressed skin, the critical failure mode is buckling due to the axial force caused by rudder bending

https://doi.org/10.1017/aer.2016.54 Published online by Cambridge University Press

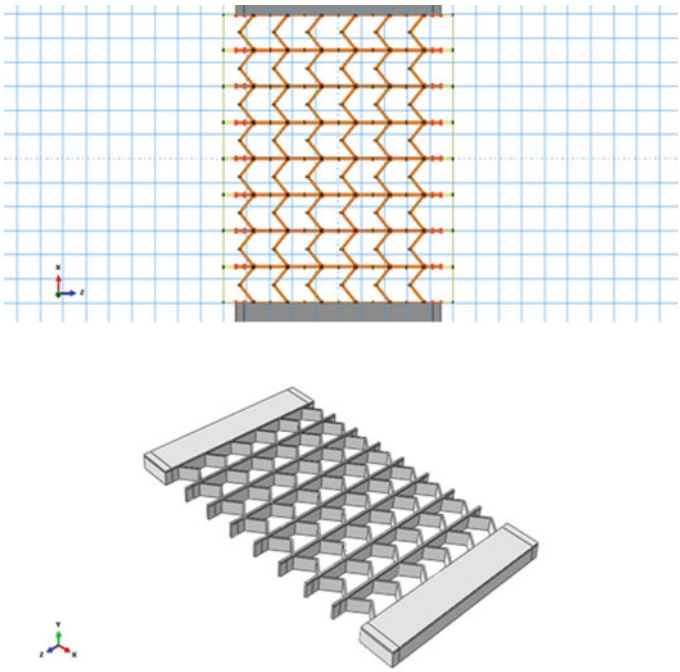


Figure 5. (Colour online) V-plane skeleton-skin panels.

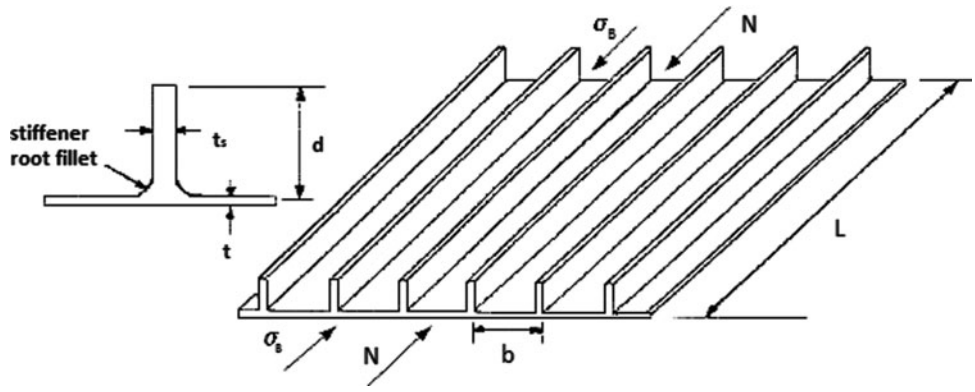


Figure 6. Reinforced skin geometry parameters.

in combination with the rudder torsion shear flow. For the tension failure mode, we derive the skin's maximum combined von Mises stresses and compare them with rupture allowable ones. The skins are modelled as constituted by single-ply orthotropic material; therefore, due to the grid-cell skeleton configuration of the skins, it is necessary to determine the equivalent material properties. The geometric parameters involved in the skins' strength analysis are t (basic cell thickness), t_s (stringer web thickness), b (distance between adjacent stringers) and stringers height d (Fig. 6)).

The second group of parameters for skins is related to the configuration of the skeleton itself. The skeleton is not rigid chord-wise but presents a span-wise stiffness due to the various

https://doi.org/10.1017/aer.2016.54 Published online by Cambridge University Press

stringers. We derive a number of parameters on which the effective stiffness of the skeleton depends. Different close-to-zero Poison panels configurations based on two cell geometric parameters and topology alternatives have been pre-selected to search for the lower weight configuration and at the same time fulfil strength and stiffness requirements.

The allowable load flows on the rudder skins to perform the compression strength analysis have been obtained by means of the Farrar theory[16] programmed into MATLAB. This code takes as input the internal compression loads and the geometry constraints and performs calculations that yield an optimum set of geometrical parameters for the structure.

Farrar's theory states that the optimum structure is one in which the compression stresses at the beginning of the initial local buckling σ_B match the corresponding Euler buckling as a column σ_E. In this way, when the local buckling is induced, the global buckling of the entire skin starts. These stresses are given by these equations:

$$\sigma_B = \frac{\sigma_B}{\sigma_0} f_1\left(\frac{A_S}{bt}, \frac{t_S}{t}\right) 3.6\, E \left(\frac{t}{b}\right)^2, \quad \ldots (17)$$

$$\sigma_E = \frac{\pi^2 E}{L_{eq} 2}\left[\frac{\rho}{b} f_2\left(\frac{A_S}{bt}, \frac{t_S}{t}\right)\right]^2 b^2 \quad \ldots (18)$$

The parameters involved are represented on Fig. 6:

- A_s is the area of the rectangular section of stringers.

$$A_s = d \times t_s \quad \ldots (19)$$

- L_{eq} is the equivalent length of the skins and stringers, since it is assumed that ribs provide a stable support it is the pitch between ribs.
- E_{rev} is the modulus equivalent for a one-ply material
- σ_0 is the skin buckling as a plate

$$\sigma_0 = 3.6E\left(\frac{t}{b}\right)^2 \quad \ldots (20)$$

The Farrar theory also defines a reference stress σ_{ref} and a mean stress σ_m because the reinforced skin stress distribution is not uniform. The Farrar factor, F, is defined as the ratio between the mean and reference stresses, concluding that the higher the value of F, the most optimum the structure results. The expressions are:

$$\sigma_m = \frac{Nb}{A_S + bt}, \quad \ldots (21)$$

$$\sigma_{ref} = \sqrt{\frac{N \times E}{L_{eq}}}, \quad \ldots (22)$$

$$F = \frac{\sigma_m}{\sigma_{ref}} = \sigma_m \sqrt{\frac{L_{eq}}{N \times E}} \quad \ldots (23)$$

https://doi.org/10.1017/aer.2016.54 Published online by Cambridge University Press

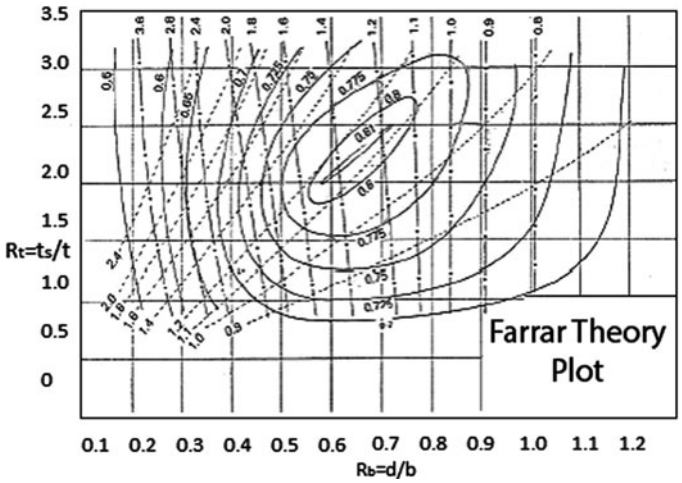


Figure 7. Original Farrar theory plot.[16]

If we now imposed the condition of simultaneous local and global buckling, and both are equal to average stress: $\sigma_m = \sigma_B = \sigma_E$, then F is obtained as a solely function on the geometry parameters, specifically the parameters t_s, t, b and d.

The problem of applying this theory to a real case is the combination between equations and graphs. In this study, the graphs for each Farrar factor F level have been MATLAB-modelled. Figures 7 and 8 show original Farrar plots and the MATLAB plots. So, starting with known values of $R_b = d/b$ and $R_t = t/t_s$ and the graph $F = f(R_b, R_t)$, the values of all the other geometric parameters as functions of L_{eq} and the Young modulus E have been derived, averaging between the stringers and the skin:

$$t = \frac{1}{F\,(1 + R_b R_t)} \left(\frac{N \times L_{eq}}{E} \right)^{1/2}, \qquad \ldots (24)$$

$$b = 1.103 \frac{\sqrt{F}\,(1 + R_b R_t)}{\left[R_b^3 R_t\,(4 + R_b R_t) \right]^{1/2}} \left(\frac{N \times L_{eq}}{E} \right)^{1/2}, \qquad \ldots (25)$$

$$F^4 = \frac{\sigma_m^4}{\frac{N \times E}{L_{eq}}} = \frac{\sigma_m^2 \sigma_B \sigma_E}{\frac{N \times E}{L_{eq}}} = \ldots = \frac{\sigma_B}{\sigma_0} \left(\frac{A_S}{bt}, \frac{t_S}{t} \right) 3.6\pi^2 \left(\left[\frac{\rho}{b} \left(\frac{A_S}{bt}, \frac{t_S}{t} \right) \right] \right)^2 \frac{1}{\left(\frac{A_S}{bt} + 1 \right)} \qquad \ldots (26)$$

The skin results are included in Table 3. These results correspond to the optimum minimum weight and geometry of an equivalent single-layer panel.

2.3 Chord-wise skins

The chord-wise skin can deform as a skeleton up to certain level to accommodate the morphing. To characterise the strength, the maximum stress at break under tension loading is considered, and for the stiffness, just the tensile stiffness. This simplifies the skeleton characterisation to only two equations.

https://doi.org/10.1017/aer.2016.54 Published online by Cambridge University Press

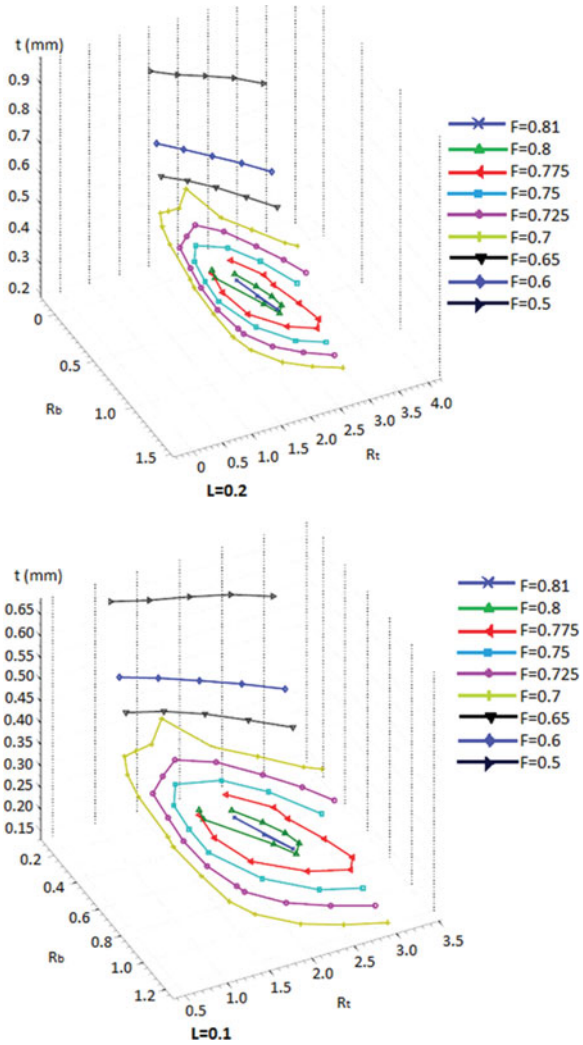


Figure 8. (Colour online) Farrar theory plot and MATLAB results for two different lengths.

An equivalent material of constant thickness is considered[17] to obtain the properties of the cell-based skeleton. The skeleton is a three-direction orthotropic structure. In- plane mechanical properties are determined by 5 parameters: E_1, E_2, G_{12}, υ_{12} and υ_{21} and out of plane by other 7: E_3, G_{13}, $G_{(23,)}$ υ_{13}, υ_{31}, υ_{23} and υ_{32}.

To calculate the elastic module of the new double-C configuration, a number of assumptions have been considered. The Euler-Bernoulli theory should be applicable. This means that the deformations are sufficiently small so that the sections originally perpendicular to the line of deformation remain perpendicular after deformation. There is also a relationship between the span-wise thickness of the stringers obtained in the previous section and the chord-wise thickness of the springs: $t_m = k_s \times t_s$. Also, this thickness is much smaller than the characteristic length of the spring $t_m/L_m \ll 1$. Using symmetry conditions, the analysis is simplified by imposing the appropriate boundary conditions in each case, so the point on the

https://doi.org/10.1017/aer.2016.54 Published online by Cambridge University Press

Table 3
Skins results

t_s (mm)	d (mm)	q_{cr} (N/m)	σ_{VM} (MPa)
5.7	55.4	30,500	27.0
F	R_b	R_t	t/ b (mm)
0.75	0.6	1.25	4.6/92.4

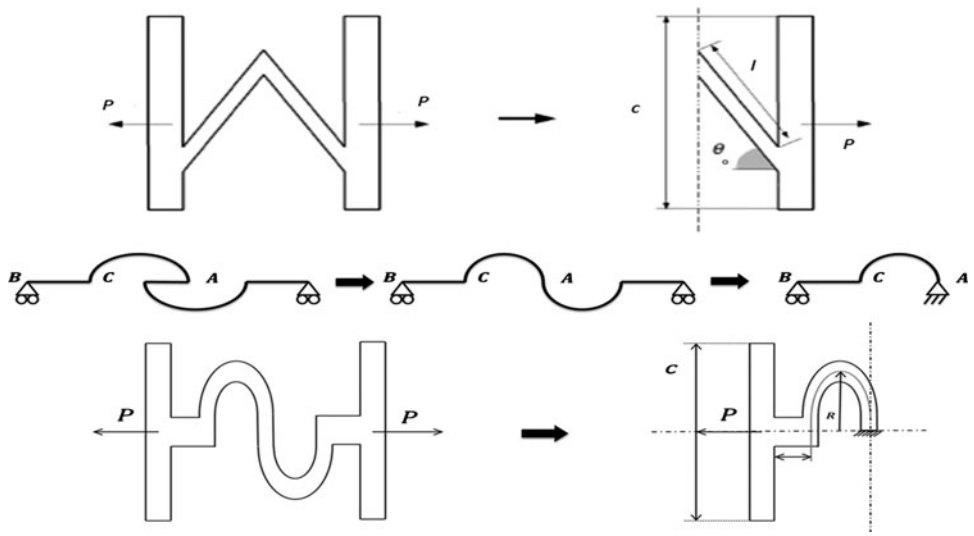


Figure 9. V-straight and double-C parameters.

axis of symmetry will be called A and the one located in the stringer will be called B. The following equations that provide the values of the linear displacements at point B (u_B, υ_B) and the rotation angle θ_B as a function of these values on point A are applied in Fig. 9.

$$u_B = u_A + \theta_A (y_B - y_A) - \int_A^B \frac{M_f(s)}{E_0 I_z} (y_B - y)\, ds, \quad \ldots (27)$$

$$\upsilon_B = \upsilon_A + \theta_A (x_B - x_A) - \int_A^B \frac{M_f(s)}{E_0 I_z} (x_B - x)\, ds, \quad \ldots (28)$$

$$\theta_B = \theta_A + \int_A^B \frac{M_f(s)}{E_0 I_z} ds \quad \ldots (29)$$

Based on the above equations, the value of the elastic module E_1 is obtained. To do so, we previously derived the value of the displacement at point B by imposing the equations of static equilibrium under a concentrated force P. We are then required to take advantage of the boundary conditions to determine the value of hyperstatic variables:

$$u_A = 0, \quad \ldots (30)$$

https://doi.org/10.1017/aer.2016.54 Published online by Cambridge University Press

$$v_A = 0, \quad \ldots (31)$$

$$v_B = 0, \quad \ldots (32)$$

$$\theta_B = 0, \quad \ldots (33)$$

$$H_A + P = 0, \quad \ldots (34)$$

$$V_A + V_B = 0, \quad \ldots (35)$$

$$M_B + V_A (2R + l) = 0, \quad \ldots (36)$$

Then the hyperstatic unknown M_B is selected. The bending moment, which is then introduced into the above equations, is defined within two sectors: from A to C and from C to B.

For A to C: $s \ (0 , \ l)$

$$M_f (s) = M_B \quad \ldots (37)$$

For C to B: $\gamma \ (0 , \ 2\pi)$

$$M_f (\gamma) = M_B + PR \sin \gamma \quad \ldots (38)$$

The system is solved, first expressing θ_A as a function of M_B and rest of parameters of the problem: E, I, l, R and P.

$$\theta_A EI = M_B (l + 2R) + 2PR^2, \quad \ldots (39)$$

$$\theta_B EI = \theta_A EI - \int_0^{l+2R} M_B ds - \int_0^{\pi} PR^2 \sin \gamma d\gamma = 0, \quad \ldots (40)$$

Then u_B is derived as a function of M_B after imposing two conditions:

$$u_A = 0, \quad \ldots (41)$$

$$y_A = y_B, \quad \ldots (42)$$

$$EIu_B = \int_0^{\pi} (M_B + PR \sin \gamma) R^2 \sin \gamma d\gamma, \quad \ldots (43)$$

$$EIu_B = R^2 \left(2M_B + \frac{PR\pi}{2} \right) \quad \ldots (44)$$

https://doi.org/10.1017/aer.2016.54 Published online by Cambridge University Press

To solve the problem, it is necessary to calculate the value of M_B. For this, it is assumed:

$$v_A = v_B = 0, \quad \ldots (45)$$

$$x_A = 2R + l, \quad \ldots (46)$$

$$x_B = 0, \quad \ldots (47)$$

$$-EI\theta_A (2R + l) - \int_0^l M_B s ds - \int_0^{\pi} M_B (R\cos\gamma + l) R d\gamma - \int_0^{\pi} PR^3 \sin\gamma\cos\gamma d\gamma = 0 \quad \ldots (48)$$

That yields:

$$M_B = \frac{-2PR^2 (2R + l)}{(l + 2R)^2 + l\left(R\pi + \frac{l}{2}\right)} \quad \ldots (49)$$

Then:

$$u_B = \frac{R^2}{EI}\left(\frac{-4PR^2 (2R + l)}{(l + 2R)^2 + l\left(R\pi + \frac{l}{2}\right)} + \frac{PR\pi}{2}\right) \quad \ldots (50)$$

Therefore,

$$\varepsilon_B = \frac{R^2}{EI (2R + l)}\left[\frac{-4PR^2 (2R + l)}{(l + 2R)^2 + l\left(R\pi + \frac{l}{2}\right)} + \frac{PR\pi}{2}\right] \quad \ldots (51)$$

Since

$$\sigma = \frac{P}{dc} = E_{1DC}\varepsilon_B, \quad \ldots (52)$$

where d is the height of the stringers and c is a new parameter that defines the distance between

https://doi.org/10.1017/aer.2016.54 Published online by Cambridge University Press

springs. Thus,

$$E_{1DC} = \frac{EI}{dc} \frac{(2R+l)}{R^2 \left[\frac{-4R^2(2R+l)}{(l+2R)^2 + l\left(R\pi + \frac{l}{2}\right)} + \frac{R\pi}{2} \right]} \quad \ldots (53)$$

We apply this method to the case of the V-straight configuration, whose geometry can be seen in Fig. 9:

$$E_{1VS} = \frac{12EI}{dc} \frac{\cos\theta_0}{l^2 \sin{\theta_0}^2} \quad \ldots (54)$$

The division of these two last expressions yields this comparison ratio:

$$\frac{E_{1VS}}{E_{1DC}} = \frac{12\cos\theta_0 R^2 \left[\frac{-4R^2(2R+l)}{(l+2R)^2 + l\left(R\pi + \frac{l}{2}\right)} + \frac{R\pi}{2} \right]}{{l_v}^2 \sin{\theta_0}^2 (2R + l_v)} \quad \ldots (55)$$

Then, after an approximation method, the conclusion is as follows:

$$\frac{E_{1VS}}{E_{1DC}} \approx \frac{1}{9} \quad \ldots (56)$$

It is clear that the double-C configuration is one order of magnitude stiffer chord-wise than the V-straight configuration.

The elastic modulus value E_2 is almost the same for both configurations since it depends only on the number of stringers, which in turn depends on the chord length and a shape that can be considered equal in both cases. Consequently, the relationship between module E_2 and the equivalent material is proportional to the area ratio:

$$\frac{E_2}{E} = \frac{A_s}{A_{eq}} = \frac{t_s}{b} \ll 1 \quad \ldots (57)$$

In consequence:

$$E_{2VS} = E_{2DC} = \frac{t_s}{b} E \ll E \quad \ldots (58)$$

Similarly to E_2, the elastic modulus E_3 is proportional to the area, and thus considerably smaller than the case of the skeleton compared to the modulus of the material itself. In the case of the double-C configuration, the equivalent area can be calculated as the sum of the different zones, the stringers, the two straight sections and the two areas in C:

$$A_{eq} = 1.15 t_s (c + k_s (2l + 2\pi R)) \quad \ldots (59)$$

where k_s represents the ratio between the span-wise stringer thickness divided by the springs' chord-wise thickness. Moreover, it is multiplied by a factor of 1.15 to take into account the

https://doi.org/10.1017/aer.2016.54 Published online by Cambridge University Press

Table 4
V-straight configuration, springs parameters

n_c	$\theta_0(^\circ)$	$l(mm)$	$c(mm)$
6	59, 5	10	106.5
$K(N/m)$	$E_1(MPa)$	$E_2(GPa)$	$E_3(GPa)$
55, 4	0, 175	0, 231	0, 445

part of the two 'C' shapes that have been previously neglected. The area ratio is as follows.

$$\frac{E_3}{E} = \frac{A_{eq}}{A_s} = \frac{1.15t_s\,(c + k\,(2l + 2\pi R))}{cb} \quad \ldots(60)$$

In this equation, the numerator is approximately proportional to $t_s(c + b)$ and about the same order as c and b. Therefore E_3 and E_2 are of the same order.

$$E_{3VS} \approx E_{3DC} \approx \frac{t_s}{b}E \ll E \quad \ldots(61)$$

All the terms to define the geometry related to the equivalent springs of the two configurations have been derived.

The final calculations of the springs' mechanical characteristics, minimising the modulus E_1 and maximising the two others E_2, E_3, are now performed. These are based on the following additional considerations:

- The number of springs in the direction of the span is the distance between ribs divided between the parameter *c,* rounded.
- The width of the spring chord-wise is equal to *b.* This restricts the value of other parameters.
- The definition of K, as the stiffness associated with the springs, is performed. The calculation of the individual stiffness of each spring as the product of the modulus of rigidity E_1 multiplied by the height of the stringers d and the width of each spring c and divided by the length of each spring b is finally obtained. Then, associating the springs in parallel and in series depending on the number of springs in the direction of the chord n_c and span-wise n_e results in:

$$K = \frac{n_c}{n_e}k = \frac{n_c}{n_e}\,\frac{E_1 dc}{b} \quad \ldots(62)$$

From the standpoint of structural integrity, a geometry that makes the maximum tension stress σ as small as possible to avoid rupture, as well as lower average compression stress to avoid local or global buckling, is the goal of this part of the analysis. Tables 4 and 5 present the final values for the two configurations under study.

https://doi.org/10.1017/aer.2016.54 Published online by Cambridge University Press

Table 5
Double-C configuration, springs parameters

n_c	$\theta_0(^\circ)$	$l(mm)$	$c(mm)$
6	n/a	17	106.5
$K(N/m)$	$E_1(MPa)$	$E_2(GPa)$	$E_3(GPa)$
124,7	1, 842	0, 231	0,388

3.0 RESULTS AND DISCUSSION

The structural feasibility of this design is verified by integrating the morphing skin structure in solid CATIA 5 models for cinematic mechanical analysis and simulation. Figure 10 shows some of the geometrical details of these 3D models.

The study is completed with numerical models based on the finite element method code Abaqus, taking into account the obtained geometrical parameters, the boundary conditions and the applied loads. The utilisation of Abaqus for solving similar problems is well documented in the literature. The renewable energy wind industry provides examples for studying morphing in wing blades with Abaqus models[7,9,18]. Recently, Abaqus models of human tissues that morph to different shapes have been developed[19]. The complexity of combining large deformations, composite materials and novel actuation systems has also been recently studied with help of Abaqus models[4,20].

Abaqus FEM models with rough meshing but enough detail to test the two types of skeletons excluding the exterior elastomeric skin have been constructed. Then the mesh is refined to test the full skin for the two configurations. The model has been made for three consecutive ribs, so the simulation results in the central rib are as representative as possible of the typical loads that most rudder ribs withstand. The geometry of the second rib is considered because, as shown before, it has the highest internal loads. This model is cylindrical and does not consider the variation of the chord along the span. This simplification is proven in industrial practice and the results correlated with tests are good for a detailed analysis around a rib (Fig. 11).

The applied loads to the models correspond to the previously indicated of one engine out condition with additional enforced displacements due to a 30° rudder rotation.

3.1 V-straight configuration results

Figure 12 shows the Von Mises stress on a scale between 8 KPa and 3.6 MPa (material elastic limit). This scale will be maintained for the rest of the stress results. As is shown, there are areas of particular stress concentration, particularly in the junction zones between the stringers and the chord 'springs'. The most critical areas are the joint of the skeleton with the trailing edge continuous spar, and the first fitting rib clamping area. This is due to the transmitted enforced displacements through the articulated ribs to the skeleton and the stiff trailing-edge member. This result is repeated in all cases. This feature is solved with adequate reinforcements.

The maximum deformations are on the order of 5% (Fig. 13); this scale will remain constant for the rest of the strain plots.

https://doi.org/10.1017/aer.2016.54 Published online by Cambridge University Press

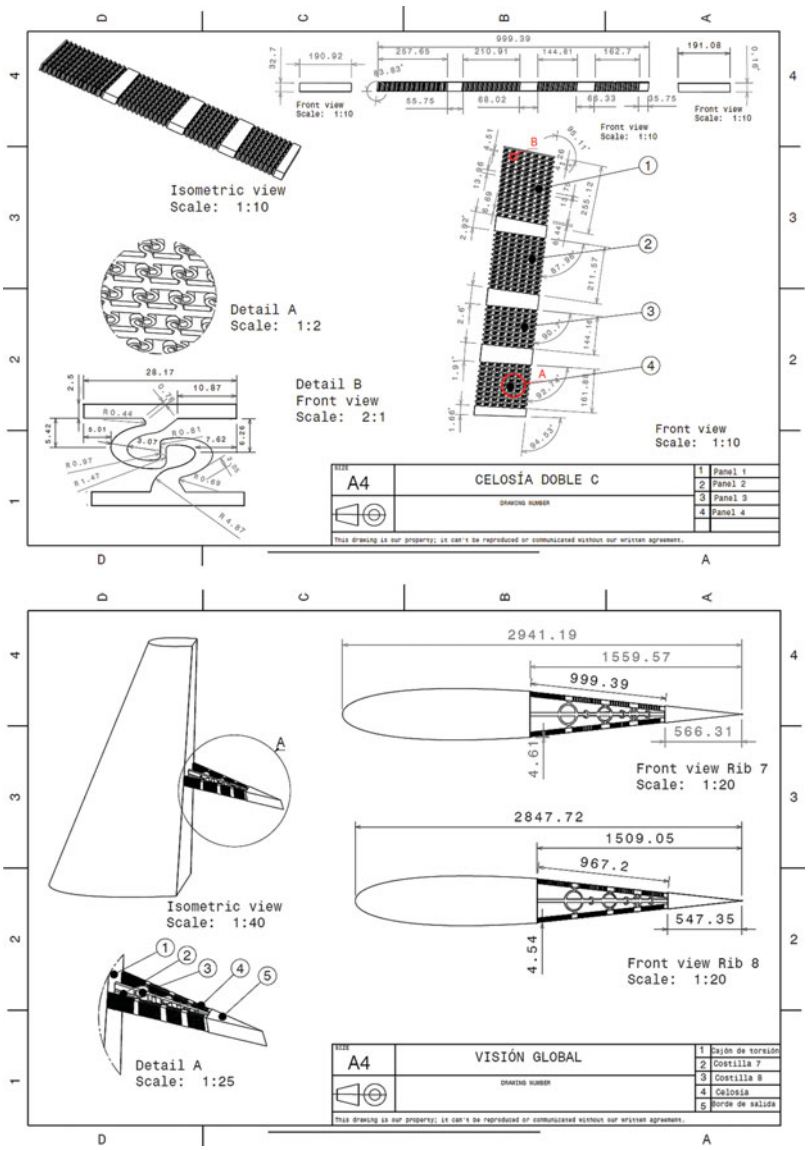


Figure 10. (Colour online) Double-C geometrical definition.

3.2 Double-C configuration results

The results for this configuration are included in Fig. 14. The behaviour is similar to the 'V' configuration, with greater differences in the chord spring stresses and strains. A 90% reduction of maximum von Mises stress in relation to the V-straight configuration is derived.

Looking more closely at one of the springs (Fig. 15), the rotation is clearly observed in the central area. This is the angle θ_A formed by the line that connects the two C shapes with the chord-wise axis. This rotation is in the order of the angle between the local plane normal with the vertical.

https://doi.org/10.1017/aer.2016.54 Published online by Cambridge University Press

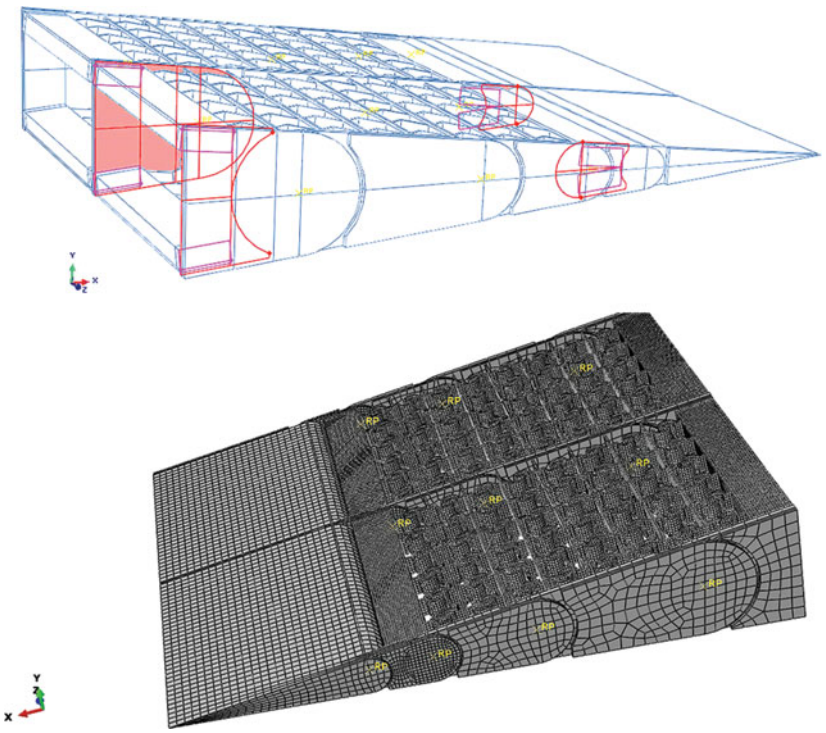


Figure 11. (Colour online) Abaqus FEM 2.5D rudder model.

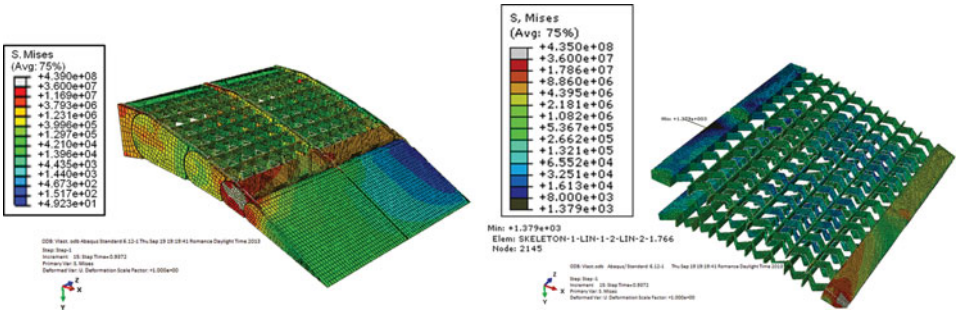


Figure 12. V-straight FEM von Mises stress (N/m^2).

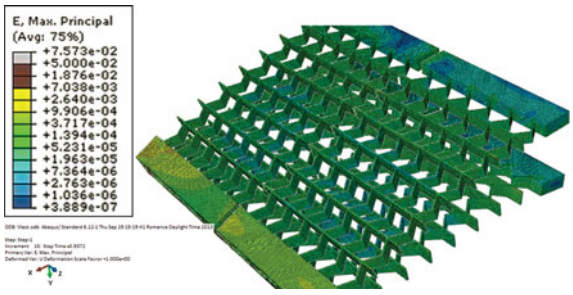


Figure 13. (Colour online) V-straight FEM strains ($\mu\epsilon$).

https://doi.org/10.1017/aer.2016.54 Published online by Cambridge University Press

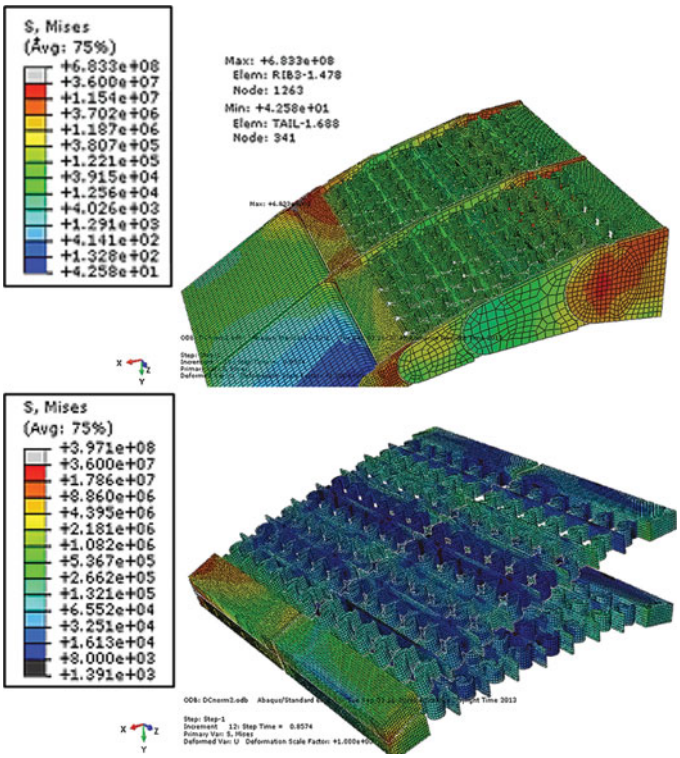


Figure 14. Double-C FEM von Mises stress (N/m^2).

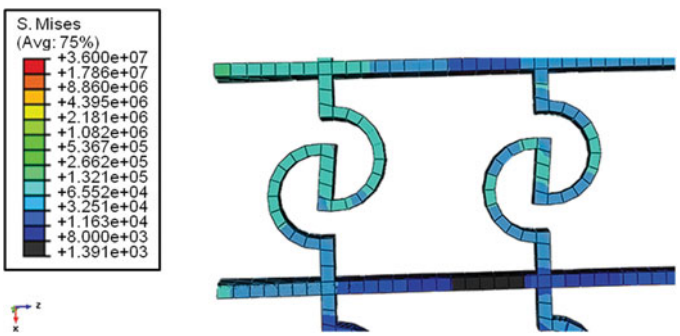


Figure 15. (Colour online) Double-C FEM spring rotation detail, von Mises stress (N/m^2).

It is relevant to note that these stresses are much less concentrated than in the previous configuration. This is critical from the point of view of the durability of the structure and compensates for its greater stiffness. These concentrations need to be further studied from a fatigue point of view. Complete fatigue studies from a multi-disciplinary approach is important in aircraft design with novel morphing devices[21,22] specially with thermo-mechanical coupling[23] and the effect of chemical resistance[24]. Figure 16 includes the skeletons strains.

https://doi.org/10.1017/aer.2016.54 Published online by Cambridge University Press

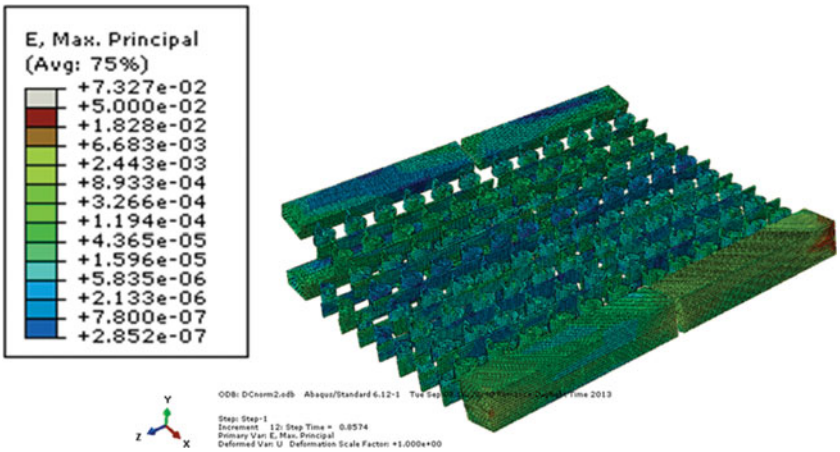


Figure 16. (Colour online) Double-C FEM strains ($\mu\epsilon$).

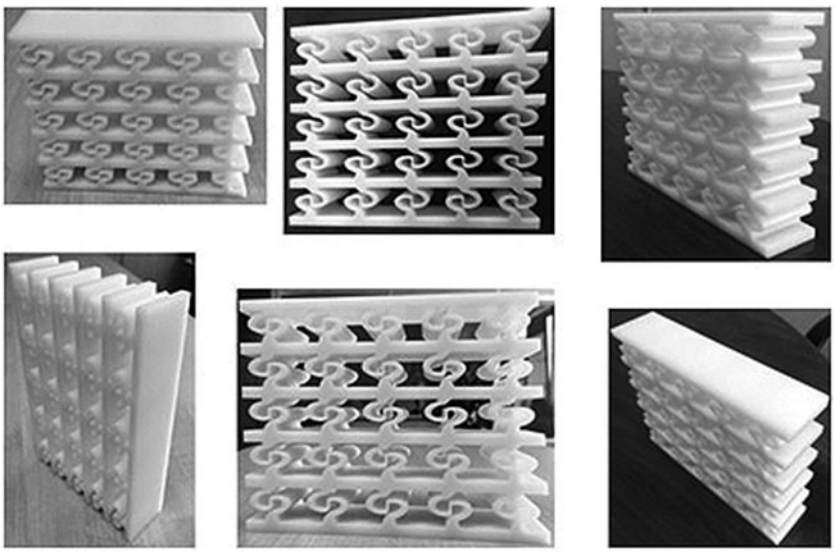


Figure 17. Pictures of 3D printed element.

A double-C representative panel has been produced by an additive layer manufacturing process using the selected material VisiJet M 3X. Figure 17 includes some pictures of the manufactured specimen.

The 3D printer is a ProJet 7000 MP based on stereolithography technology. The amount of material used is 210 g. The time consumed is around 7 hours.

4.0 CONCLUSIONS

This study includes the development of an analytical model to design an adaptable skin with multiple parameters, constraints and configurations. The equations that relate morphing

https://doi.org/10.1017/aer.2016.54 Published online by Cambridge University Press

skin 3D printable skeleton mechanical properties with actual zero Poisson cellular panels' geometry and material have been obtained. Based on the obtained values, it is concluded that the design is functionally feasible and structurally compliant for aircraft structures applications from static strength point of view. In particular, this study presents some remarks:

- The so called double-C configuration has been proved to improve the V-straight configuration in relation to the rudder functional requirements.
- The selection of materials is critical to achieve a structurally compliant solution.
- The resultant skin skeleton elastic modules have to be large enough to withstand the internal loads but not so big that the required actuators forces are beyond current available commercial servomotor during the deformation process.

Further studies are required to search for more adequate 3D printable materials to be processed by additive layer manufacturing means or similar. In particular, the characterisation of fatigue life and the effect of relevant environment are pending for future work, as well as a study of the highly deformable material and its integration to the skins for non-permeability purposes.

The current commercially available 3D printing machines present a limit to critical dimensions, in particular the size of the panels, being the maximum size currently available around 0.5 m. The current available resolutions of the 3D printable elements are not affecting the geometrical definition of the highly orthotropic panels, but when more miniaturisation of the design is required, this resolution could be a limiting factor on the design. This potential issue might be further studied in the future at similar miniature 3D printed elements.

REFERENCES

1. CASTILLO-ACERO, M.A., CUERNO-REJADO, C. and GÓMEZ-TIERNO, M.A. Aerodynamic modelling for a morphing rudder, Proceedings of the 2014 RAES Aerodynamics Conference, 22-24 July 2014, RAES Bristol, UK.
2. BARBARINO, S., BILGEN, O., AJAJ, R.M., FRISWELL, M.I. and INMAN, D.J. A review of morphing aircraft, *J Intelligence Materials, Systems and Structures*, August 2011, **22**, (9), pp 823-877.
3. SOFLA, A.Y.N., MEGUID, S.A., TAN, K.T. and YEO, W.K. Shape morphing of aircraft wing: status and challenges, *Materials and Design*, March 2010, **31**, (3), pp 1284-1292.
4. PORTELA, P., CAMANHO, P., WEAVER, P. and BOND, I. Analysis of morphing, multi stable structures actuated by piezoelectric patches, *Computers and Structures*, February 2008, **86**, (3-5), pp 347-356.
5. MONNER, H.P. Realization of an optimized wing camber by using form variable flap structures, *Aerospace Science Technology*, **5**, (7), pp 445-455.
6. PECORA, R., AMOROSO, F. and MAGNIFICO, M. Design and experimental validation of a morphing wing flap device, Proceedings of the 6th ECCOMAS Conference on Smart Structures and Materials (SMART'13), 24-26 June 2013, Politecnico di Torino, Turin, Italy.
7. LACHENAL, X., DAYNES, S. and WEAVER, P.M. Review of morphing concepts and materials for wind turbine blade applications, *Wind Energy*, February 2013, **16**, pp 283-307.
8. DAYNES, S. and WEAVER, P.M. A morphing trailing edge device for a wind turbine, *J Intelligence Materials, Systems and Structures*, March 2012, **23**, (6), pp 691-701.
9. DAYNES, S. and WEAVER, P.M. Design and testing of a deformable wind turbine blade control surface, *Smart Materials and Structures*, **21**, (10), pp 105–119.
10. SCHWEIGER, J. and KRAMMER, J. Active aircraft and its impact on structure flight control systems design, RTO AVT Specialists' Meeting on Structural Aspects of Flexible Aircraft, 18-20 October 1999, Ottawa, Ontario, Canada.
11. SCHWEIGER, J. Active aeroelastic aircraft concepts, RTA-AVT-86 Technical Course, 25-29 March 2002, METU, Ankara, Turkey.

https://doi.org/10.1017/aer.2016.54 Published online by Cambridge University Press

12. GOMEZ, J.C. and GARCIA, E. Morphing unmanned aerial vehicles, *Smart Materials and Structures*, **20**, (10), p 103001 (16pp).
13. VOCKE, R.D., KOTHERA, C.S., WOODS, B.K.S., BUBERT, E.A. and WERELEY, N.M. One dimensional morphing structures for advanced aircraft, Phase I SBIR Project from NASA Langley Research Center, contract number NNX09CF06P, 2007.
14. 3D systems Corporation, Professional 3D Printers Productivity Precision, available on line, accessed 2 March 2014, http://www.3dsystems.com.
15. BUBERT, E.A. Highly Extensible Skin for a Variable Wing-Span Morphing Aircraft Utilizing Pneumatic Artificial Muscle, *MSc Thesis, University of Maryland*, USA, 2009.
16. FARRAR, D.J. Investigation of skin buckling, ARC R&M No. 2652, 1953.
17. VOS, R. Mechanics and applications of pressure adaptive honeycomb, *PhD Thesis, University of Kansas*, USA, 2009.
18. CHEN, J., WANG, Q., SHEN, W.Z., PANG, X., LI, S. and GUO, X. Structural optimization study of composite wind turbine blade, *Materials and Design*, April 2013, **46**, pp 247-255.
19. WANG, H.M., GAO, H., LUO, X.Y., BERRY, C., GRIFFITH, B.E., OGDEN, R.W. and WANG, T.J. Structure-based finite strain modeling of the human left ventricle in diastole, *Int J Numerical Methods in Biomedical Engineering*, June 2013, **29**, pp 83-103.
20. DIACONU, C.G., WEAVER, P.M. and MATTIONI, F. Concepts for morphing airfoil sections using bi-stable laminated composite structures, *Thin-Walled Structures*, June 2008, **46**, (6), pp 689-701.
21. KOTA, S., HETRICK, J. and OSBORN, R. Design and application of compliant mechanisms for morphing, *Smart Structures and Materials*, June 2003, **5054**, (734), pp 24-33.
22. VASISTA, S., TONG, L. and WONG, K.C. Realization of morphing wings: a multidisciplinary challenge, *J Aircraft*, January 2012, **49**, (1), pp 11-28.
23. JEE, S. Development of morphing aircraft structures using SMP, AFIT/GSE/ENV/10-M02, Air Force Institute of Technology Graduate School of Engineering and Management, Wright-Patterson Air Force Base, Ohio, US, 2010.
24. THILL, C., ETCHES, J., BOND, I., POTTER, K. and WEAVER, P. Morphing skins, *Aeronautical J*, March 2008, **112**, (1129), pp 117-139.

https://doi.org/10.1017/aer.2016.54 Published online by Cambridge University Press